

Document downloaded from:

<http://hdl.handle.net/10251/121756>

This paper must be cited as:

García-Fayos, J.; Balaguer Ramirez, M.; Baumann, S.; Serra Alfaro, JM. (2018). Dual-phase membrane based on  $\text{LaCo}_{0.2}\text{Ni}_{0.4}\text{Fe}_{0.4}\text{O}_{3-x}\text{-Ce}_{0.8}\text{Gd}_{0.2}\text{O}_{2-x}$  composition for oxygen permeation under  $\text{CO}_2/\text{SO}_2$ -rich gas environments. *Journal of Membrane Science*. 548:117-124. <https://doi.org/10.1016/j.memsci.2017.11.006>



The final publication is available at

<http://doi.org/10.1016/j.memsci.2017.11.006>

Copyright Elsevier

Additional Information

# Dual-phase membrane based on $\text{LaCo}_{0.2}\text{Ni}_{0.4}\text{Fe}_{0.4}\text{O}_{3-x}$ - $\text{Ce}_{0.8}\text{Gd}_{0.2}\text{O}_{2-x}$ composition for oxygen permeation under $\text{CO}_2/\text{SO}_2$ -rich gas environments

Julio Garcia-Fayos<sup>1</sup>, María Balaguer<sup>1</sup>, Stefan Baumann<sup>2</sup>, José M. Serra<sup>1,\*</sup>

<sup>1</sup>*Instituto de Tecnología Química (Universitat Politècnica de València – Consejo Superior de Investigaciones Científicas), Av. Naranjos s/n, E-46022 Valencia (SPAIN)*

<sup>2</sup>*Forschungszentrum Jülich GmbH, Institute of Energy and Climate Research-IEK-1, Leo-Brandt-Str. 1, D-52425 Jülich, Germany*

\* corresponding author: jmserra@itq.upv.es

## Abstract

A dual-phase material with high ambipolar conductivity composed by the perovskite  $\text{LaCo}_{0.2}\text{Ni}_{0.4}\text{Fe}_{0.4}\text{O}_{3-\delta}$  (LCNF) as the electronic phase and the fluorite  $\text{Ce}_{0.8}\text{Gd}_{0.2}\text{O}_{2-\delta}$  (CGO20) as oxide-ion conductor is proposed for use as oxygen transport membrane. The chemical compatibility between both materials depends on the synthesis method, i.e. one-pot sol-gel synthesis leads to the formation of the fluorite and the perovskite phases, as well as a third NiO-based phase. The formation of this last phase can be avoided by previously stabilizing the phases separately. The composite material shows high electrical conductivity, i.e.,  $7.25 \text{ S cm}^{-1}$  at  $800 \text{ }^\circ\text{C}$  for LCNF-CGO20 with NiO impurity, and  $2.6 \text{ S cm}^{-1}$  at  $800 \text{ }^\circ\text{C}$  for LCNF-CGO20. A maximum oxygen flux,  $J(\text{O}_2)$ , of  $0.74 \text{ ml} \cdot \text{min}^{-1} \cdot \text{cm}^{-2}$  is obtained at  $1000 \text{ }^\circ\text{C}$  for a surface-activated membrane in Air/Ar gradient at ambient pressure. The membranes were tested under i) 30%  $\text{CO}_2$  in Ar, and ii) 250 ppm of  $\text{SO}_2$  in 30%  $\text{CO}_2$  in Ar, reproducing oxyfuel-like conditions. Oxygen flux decreases in these atmospheres, especially at temperatures below  $900 \text{ }^\circ\text{C}$ , due to competitive adsorption of these gases with the  $\text{O}_2$ . After  $\text{CO}_2$  and  $\text{SO}_2$  exposure, initial oxygen fluxes are recovered when switching back to Ar sweeping at temperatures above  $900 \text{ }^\circ\text{C}$ . Nevertheless, at temperatures  $<900 \text{ }^\circ\text{C}$  the original  $J(\text{O}_2)$  before  $\text{SO}_2$  exposure is not fully recovered and postmortem FESEM images reveal the membrane surface degradation in  $\text{SO}_2$ .

## 1. Introduction.

Oxyfuel technology in fossil-fuel power plants and other energy-intensive industries has emerged as a key technology to facilitate energy efficiency, and efficient integration of CO<sub>2</sub> capture strategies and thus minimize greenhouse emissions. Oxyfuel process realizes the fuel combustion using N<sub>2</sub>-free O<sub>2</sub>-containing gas streams, i.e. either pure oxygen or O<sub>2</sub>-enriched flue gas, instead of air. The absence of N<sub>2</sub> allows, on one hand, more efficient combustion processes minimizing NO<sub>x</sub> formation and, on the other hand, the direct CO<sub>2</sub> sequestration process. [1, 2] Oxyfuel technology implementation may be boosted by using thermally-integrated oxygen transport membranes (OTMs) to obtain O<sub>2</sub>-rich gas stream [3] instead of the established technologies, i.e. cryogenic distillation and pressure swing adsorption. In addition, this membrane technology can be used in the intensification of chemical processes, by setting up catalytic membrane reactors that enable to shift the equilibrium of the reaction to products or prevent the direct mixture of hydrocarbons and O<sub>2</sub>. [4-6]

OTMs are made of crystalline ceramic materials that must fulfil several requirements, i.e. mixed ionic electronic conductivity (MIEC) to provide high oxygen permeability, and high structural, chemical and thermo-mechanical stability. [7] Unfortunately, the doping strategies to achieve these requirements in a single-phase material usually produce opposed effects in the mentioned properties. Materials with high ambipolar conductivity ( $\sigma_{amb} = \frac{\sigma_e \cdot \sigma_i}{\sigma_e + \sigma_i}$ , where  $\sigma_i$  is the ionic and  $\sigma_e$  the electronic conductivities, respectively) are commonly vulnerable in atmospheres containing CO<sub>2</sub>, SO<sub>2</sub>, CH<sub>4</sub> and H<sub>2</sub>O, i.e. typical gas environments found in oxyfuel processes and catalytic membrane reactors. [8, 9] As an alternative, composite materials combine the best characteristics of different compounds to achieve high oxygen permeability and relatively good chemical and mechanical stability at elevated temperatures in harsh environments. These so-called dual-phase membranes are made of an electron conducting material, which allows the electron percolation, and an ionic conductor that transports oxygen ions. [10-12]

Ceramic-metal (cermet) dual-phase membranes composed of noble metals as the electronic phase and an ion conducting ceramic have been reported, although their high costs prevented further industrial consideration. [13-15] A more cost-effective alternative is to combine ceramic–ceramic (cercer) dual-phase compounds. [16] Up to date, several crystalline structures have been studied, e.g. fluorites, perovskites, spinels and rock salts. [17] Among these materials, perovskites and spinels may be used as electronic phase. [11] Fluorite materials such as yttria stabilized zirconia (YSZ) or  $Ce_{1-x}Ln_xO_{2-\delta}$  ( $Ln$ =lanthanide) are employed as oxygen conductors since they present mainly ionic conductivity, the last family finding a maximum for Gd doped ceria. [18] The selection of the composite components should take into account (i) the chemical compatibility of the two ceramic phases in intimate contact; (ii) the influence of the grain boundary, since it can either promote or block the transport of ions; and (iii) the compatibility of thermal expansion coefficient (TEC) of both compounds regarding both mechanical stability and manufacturability.

The chemical stability of doped ceria is significantly higher than that of perovskites comprising alkaline-earth metals. [18-20] Therefore, cercers composed of doped ceria fluorites and several spinels have allowed the development of  $CO_2$  stable composite membranes [21-24] as the cobalt-free spinel  $NiFe_2O_4$  (NFO) with  $Ce_{0.9}Gd_{0.1}O_{1.95}$  (CGO10) [11] or with  $Ce_{0.8}Tb_{0.2}O_{2-\delta}$  (CTO20), [10] the last one showing good performance in terms of oxygen production ( $0.2 \text{ ml} \cdot \text{min}^{-1} \cdot \text{cm}^{-2} O_2$  at  $1000 \text{ }^\circ\text{C}$  using  $CO_2$  sweep for a monolithic) and unprecedented chemical stability in wet  $CO_2$  and 1%  $SO_2$  containing atmosphere. [10, 25, 26] The combination with perovskites has also been tested. Some advantages are presented by using a MIEC as the electronic phase. Zhu et al. combined the fluorite  $Ce_{0.8}Sm_{0.2}O_{1.9}$  with the perovskite  $Sm_{1-x}Ca_xMn_{0.5}Co_{0.5}O_3$  ( $x=0$  SMC or  $x=0.2$  SMC), which permeates up to  $0.36 \text{ ml} \cdot \text{min}^{-1} \cdot \text{cm}^{-2}$  (SDC-SMC) and remained stable in  $CO_2$  sweeping. [12]

Other perovskites traditionally used as catalysts as  $LaCoO_3$ ,  $LaNiO_3$  or  $LaFeO_3$  have very high electronic conductivity even at room temperature, but exhibit negligible oxygen ion conduction at relevant operation temperatures. Besides, they are prone to decompose at certain oxygen partial pressures. [27, 28] A binary solution of them forms a single phase material that crystallizes in

orthorhombic or rhombohedral perovskite, all depending on the relative amount of Fe, Co and Ni and on the temperature. [27] The high conductivity of this family of materials makes it a good base candidate to achieve a more economic electronic phase for dual phase membranes and, since these compounds are alkaline-earth free, good chemical stability in CO<sub>2</sub> atmospheres is expected. Recently, the quasi-ternary system of LaCoO<sub>3</sub>-LaNiO<sub>3</sub>-LaFeO<sub>3</sub> has been investigated by Tietz et al. [29]. A screening upon the variation of the amount of each metal in the perovskite showed materials with high electronic conductivities and moderate thermal expansion coefficients. By adding different amounts of Co as dopant in the B-site the conductivity of the La(Ni<sub>0.5</sub>Fe<sub>0.5</sub>)<sub>1-x</sub>Co<sub>x</sub>O<sub>3-δ</sub> increases, and also changes in the oxygen exchange activity may be expected. Within this family of materials, LaCo<sub>0.2</sub>Ni<sub>0.4</sub>Fe<sub>0.4</sub>O<sub>3-δ</sub> (LCNF) shows the highest oxygen permeation rate of 0.016 ml cm<sup>-2</sup> min<sup>-1</sup> at 950 °C. [29]

In the search of a dual phase material with high ambipolar conductivity and good stability, the perovskite LCNF is proposed as the electronic phase to be combined with the Ce<sub>0.8</sub>Gd<sub>0.2</sub>O<sub>2-δ</sub> (CGO20) as oxide-ion conductor. The TEC of the parent materials (15.9×10<sup>-6</sup> K<sup>-1</sup> of LCNF [29] and 11.9×10<sup>-6</sup> K<sup>-1</sup> of CGO20) [18, 30] are within the acceptable limits for the materials compatibility (15–25%) [31]. This work is focused on the developed of dual-phase membranes made of 50 vol.% LCNF and 50 vol.% CGO (LCNF-CGO20). Several approaches on the formation of the composites have been performed to keep the phases unreacted. The material is characterized by X-Ray Diffraction (XRD), Field Emission Scanning Electron Microscopy (FESEM), and 4-point DC conductivity measurement. Oxygen permeation testing of a planar disk dense membranes was carried out in Ar, CO<sub>2</sub> and SO<sub>2</sub> sweeping gases, as a function of temperature and including thermo-chemical cycling. The stability of the cercer material after the permeation treatment was checked by XRD, and FESEM X-ray microanalysis.

## 2. Experimental.

### 2.1. Samples preparation.

$\text{LaCo}_{0.2}\text{Ni}_{0.4}\text{Fe}_{0.4}\text{O}_{3-x}$ ,  $\text{Ce}_{0.8}\text{Gd}_{0.2}\text{O}_{2-x}$  and  $\text{LaCo}_{0.2}\text{Ni}_{0.4}\text{Fe}_{0.4}\text{O}_{3-x}$ - $\text{Ce}_{0.8}\text{Gd}_{0.2}\text{O}_{2-x}$  composite powder (in a balanced 50:50 (vol.) composite formulation) were prepared by one-pot Pechini method. [10] Homogeneous solutions of metal precursors were mixed in a common aqueous solution with citric acid to form a complex and ethylenglycol. This complexation was followed by polymerization and dehydration at low temperature and, finally, the thermal decomposition of the carbonates and nitrates at 1100 °C and 1350 °C (LCNF), 1100 °C (CGO20) and 800 °C (LCNF-CGO20) during 5 hours formed the structural phases. LCNF and CGO separately synthesized, have been mixed in a 50/50 volume ratio in a ball mill during 24 h in ethanol and dried at 75 °C afterwards. Dense specimens were obtained by 125 MPa uniaxial pressing of bars (for conductivity measurements) and green disks (for oxygen permeation) and subsequent calcination at 1400, 1460 or 1500 °C for 10 h, depending on the requirements for density. For the permeation tests, the gastight composite membranes were grinded to reach a thickness of 630  $\mu\text{m}$ .

Membrane activation was performed by depositing 30  $\mu\text{m}$ -thick 50% vol.  $\text{Ce}_{0.8}\text{Gd}_{0.2}\text{O}_{2-x}$  – 50% vol.  $\text{La}_{0.8}\text{Sr}_{0.2}\text{MnO}_{3-x}$  (CGO-LSM) porous layers on both membrane sides by means of screen-printing technique. The ink was produced by mixing nanosized CGO-LSM powder (obtained by one-pot Pechini method), an organic binder (ethylcellulose) and a plasticizer in a three-roll mill to produce a homogeneous slurry. After deposition and drying at 80 °C, the layers were sintered at 1200 °C during 2 hours.

### 2.2. Characterization.

Identification of the crystalline phases of the samples was done by means of X-ray diffraction (XRD). The measurements were carried out by a PANalytical Cubix fast diffractometer, using  $\text{CuK}\alpha 1$  radiation ( $\lambda = 1.5406 \text{ \AA}$ ) and X' Celerator detector in Bragg – Brentano geometry. XRD patterns recorded in the  $2\theta$  range from 2 or 20° to 90° were analyzed using X'Pert Highscore Plus

software. The phase distribution and cell parameters were calculated after refinement by Rietveld method, using the GSAS software package. SEM and EDX using a ZEISS Ultra55 field emission scanning electron microscope were used to analyze surfaces, and cross sections of the sintered material before and after the permeation test. SEM backscattered electrons detector (BSD) was used to provide images with compositional contrast related to the averaged atomic number of the elements of each phase, and therefore different grains and element distribution to be distinguished.

Electrical conductivity measurements were conducted by standard four-point DC technique on rectangular bars of initial  $4 \times 0.5 \times 0.2 \text{ cm}^3$ , which were uniaxially pressed at 125 MPa and subsequently sintered for 10 h at 1400 to 1500 °C in air. Silver wire and paste were used for contacting electrodes. The measurements were carried out after 2 h of stabilization at 800 °C by cooling down at a rate of  $1 \text{ °C} \cdot \text{min}^{-1}$  in constant O<sub>2</sub> containing atmospheres (Linde calibrated gas mixtures checked by a YSZ oxygen sensor). The constant current was supplied by a programmable current source (Keithley 2601) and the voltage drop through the sample was detected by a multimeter (Keithley 3706).

Oxygen permeation studies were carried out in a lab-scale quartz reactor. Synthetic air (21%, vol. O<sub>2</sub>) was fed into the oxygen-rich chamber, while argon and SO<sub>2</sub>/CO<sub>2</sub> mixtures were used as sweep gases on the permeate side in a 4-end mode configuration. Both streams were fed at atmospheric pressure. Inlet gases were preheated in order to ensure the correct gas temperature for contact with the membrane surface. This is particularly important when high gas flow rates are employed. All streams were controlled individually by mass flowmeters. The temperature was measured by a thermocouple attached close to the membrane. A PID controller maintained temperature variations within 2 °C of the set point. Membrane gas leak-free conditions were achieved using gold rings, which were heated to 1060 °C for 4 h immediately prior to the measurement. The permeate was analyzed at steady state by online gas chromatography using a micro-GC Varian CP-4900 equipped with Molsieve5A, Pora-Plot-Q glass capillary, and CP-Sil modules. Membrane gas leak-free conditions were ensured by continuously monitoring the nitrogen

concentration in the product gas stream (also before and after switching to a pure O<sub>2</sub> feed). An acceptable sealing was achieved when the ratio between the oxygen flow leak and the oxygen flux was lower than 3%. The data reported here were achieved at steady state after 1 h in the reaction stream. Each test was repeated three times to minimize the analysis error. The experimental analytical error was below 0.5%.

### **3. Results and discussion.**

#### *3.1. Structural and morphological characterization.*

Figure 1 presents the XRD pattern of initial dual phase powder calcined at 800 °C after one pot Pechini synthesis. The obtained pattern shows both the fluorite and the perovskite phases forming the composite, as well as a third phase consisted of NiO. For comparison, reference cubic fluorite (Fm-3m), orthorhombic perovskite (Pnma 62) and rhombohedral NiO rock salt (R-3m) structure diffraction patterns are indicated (ICSD 290366, ICSD 182976 [30] and ICSD 166107, respectively). Rietveld refinement made on the diffraction pattern of the obtained powder indicated that, in comparison with nominal composition, the distribution of phases is reduced in perovskite and increases the fluorite and the rock salt as summarized in the Table 1.

**Table 1.** Rietveld refinement results from the XRD patterns for LCNF-(La)CGO20-Ni(Co)O sample.

|            | Cations           | Theoretical weight % | Weight % | Reference Density (g cm <sup>-1</sup> ) | Density (g cm <sup>-1</sup> ) | Cell parameter (Å)                           |
|------------|-------------------|----------------------|----------|---|-------------------------------|--|
| Fluorite   | Ce, Gd, La        | 51.25                | 59.95    | 7.22                                    | 7                             | a= 5.48573 (6)                               |
| Perovskite | La, Fe, Co,<br>Ni | 48.75                | 37.92    | 7.01[24]                                | 6.923                         | a=5.5023 (2)<br>b=5.4686 (2)<br>c=7.7795 (2) |
| Rock Salt  | Ni, Co            | 0                    | 2.13     | 6.67                                    | 6.54                          | a=2.962 (2)                                  |

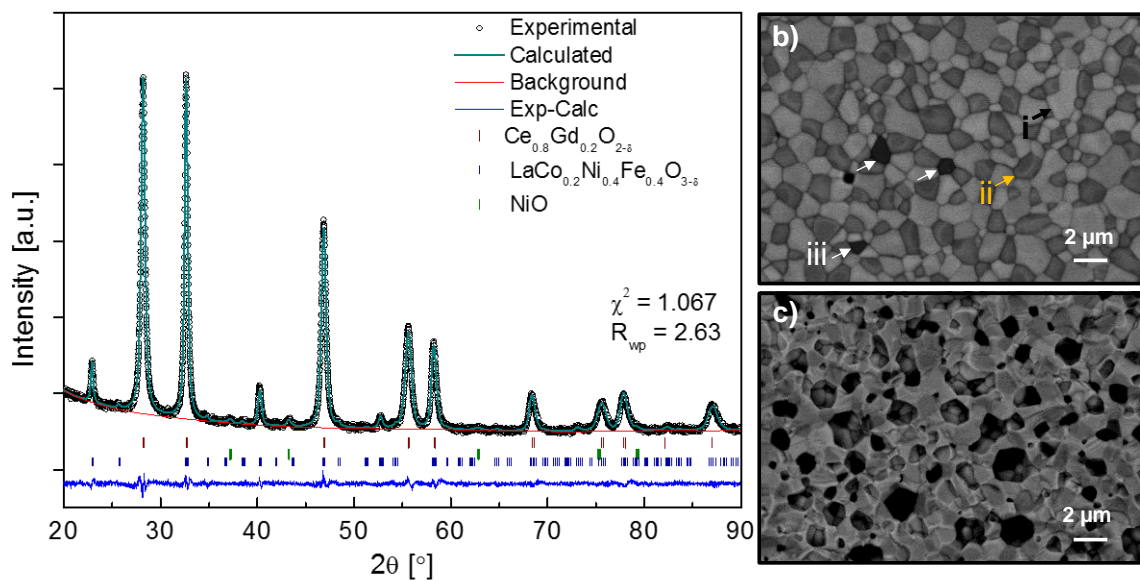


**Figure 1.** a) Rietveld analysis of X-ray diffraction data for LCNF-CGO20 powder synthesized by one-pot Pechini at 800 °C under air (LCNF-(La)CGO20-Ni(Co)O sample). The data are fitted with a mixture of CGO20, LaCo<sub>0.40</sub>Fe<sub>0.60</sub>O<sub>3-δ</sub> and NiO, b) BSD-SEM top surface and c) fracture cross-section views of a pellet sintered at 1400 °C.

The morphology of the composite specimens sintered at 1400 °C is observed in the FESEM pictures of Figure 1b and Figure 1c. The surface top-view of the as-sintered sample (Figure 1b) shows particle size homogeneity and appropriate phase distribution. The three phases observed

by XRD are distinguished, identified as i, ii, and iii. The 'i' grains are the lighter gray in the backscattered electrons image, corresponding to elements with higher z, and thus consistent with the ceria fluorite phase. EDS analysis indicates that the phase consists of Ce, Gd and La cations, which combined with the results of XRD for the fluorite phase (cell parameter of the cubic fluorite is 5.48573 (6) Å, larger than for pure CGO20), indicates that La is partly solved in the fluorite lattice. The 'ii' grains, dark gray in the picture are mainly made of La, Fe, with traces of Ni and Co, explaining that the perovskite orders in orthorhombic symmetry similarly to LaFeO<sub>3</sub> instead of rhombohedral as expected for higher Ni content [27] Finally, the grains marked as 'iii' correspond to a third phase comprising Ni, and Co in less extent. These three phases are identified in XRD. The cross-section of the membrane is depicted in Figure 1c. The specimen was gastight when tested under pressurized helium, although the closed porosity was very high (ca. 30%), suggesting that the sintering temperature is not high enough, and which is expected to have an effect in decreasing transport properties. Aiming to depict the real composition of the composite material obtained with this procedure, this material is labelled as LCNF-(La)CGO20-Ni(Co)O.

In order to avoid the reaction of the phases, another approach was followed to prepare each phase separately. In a first stage LCNF and CGO20 were synthesized separately by Pechini method and sintered at 1100 °C. At this temperature, LCNF is a mixture of orthorhombic and rhombohedral perovskite, while CGO20 is a pure cubic fluorite. A 50/50 vol% mixture of these two materials is pressed in pellets and bars and calcined at 1400 °C during 6 h. The treatment results in the formation of the three similar phases (Supporting Information Figure S1).

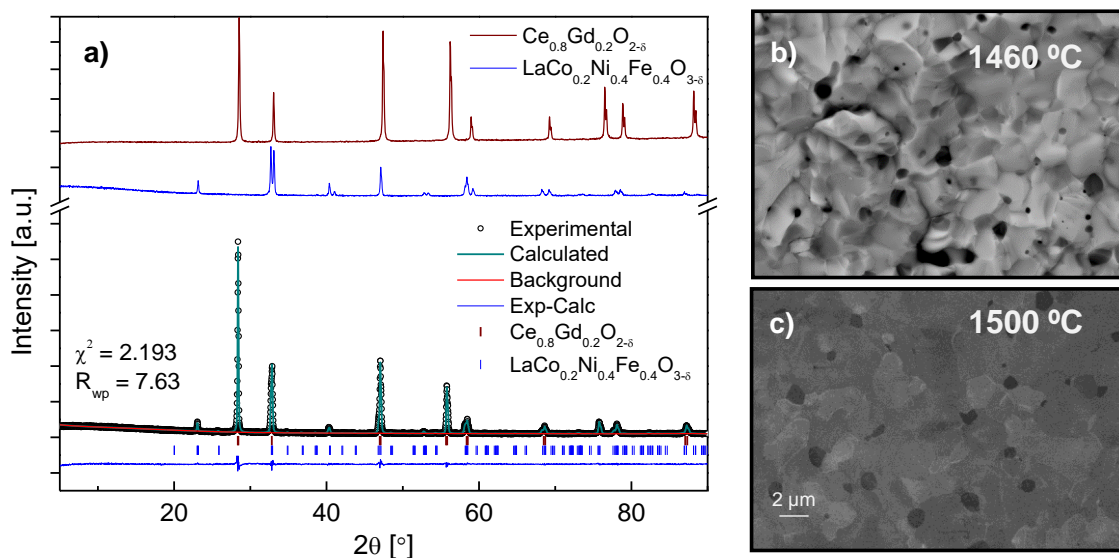


**Figure 2.** XRD patterns of rhombohedral LCNF synthesized at 1350 °C, cubic CGO20 synthesized at 1100 °C, and composite membrane made of the mentioned powders, sintered at 1460 °C (LCNF-(La)CGO20 sample), b) cross section BS-FESEM image of a membrane sintered at 1460 °C and c) cross section BS-FESEM image of a membrane sintered at 1500 °C.

The third approach was a 50/50 vol% composite consisting of LCNF calcined at 1350 °C, where a single phase rhombohedral perovskite was formed, with the aim of being more stable in contact with CGO20, which was maintained at 1100 °C to preserve sintering activity. Pressed membranes and bars were sintered at 1460 °C to achieve dense specimens, since they were not gastight at 1400 °C. Figure 2a plots the XRD patterns of the separate forming single phases and the composite at 1460 °C, where no traces of NiO are observed. However, the perovskite symmetry transformed to orthorhombic instead, and the cell parameter of the CGO20 is larger than for the single phase (Table 2), indicating that similarly to the one-pot synthesis, the ceria is dissolving other elements than Gd. Back-scattered FESEM image of the membrane cross section in Figure 2b does not reveal the presence of the Ni(Co)O phase. Moreover, material density has been improved with this third approach obtaining occlude porosity in the range of 5%. Point EDS analysis in the different grains suggests that the perovskite is mainly composed of La, Fe, Co, and Ni, but the fluorite comprises also La, therefore this material is labelled as LCNF-(La)CGO20. When increasing the temperature at 1500 °C, the sample is dense, although the rock salt phase is observed (Figure 2c).

**Table 2:** Structural information of the pristine individual phases and the final phases occurring in the composite membrane after sintering at 1460 °C. Data obtained by Rietveld refinement.

|                         | Cations                | Symmetry     | Space group | Weight % | Reference Density (g cm <sup>-3</sup> ) | Density (g cm <sup>-3</sup> ) | Cell parameter (Å)                          |
|-------------------------|------------------------|--------------|-------------|----------|---|-------------------------------|---|
| Fluorite                | CGO20: Ce, Gd          | Cubic        | Fm-3m       | 51.25    | 7.220                                   | 7.243                         | a= 5.42352 (5)                              |
| Single phase Perovskite | LCNF:<br>La, Co, Ni Fe | Rhombohedral | R3-CR       | 48.75    | 7.010                                   | 6.995                         | a=5.4426 (1)                                |
| Fluorite in composite   | Ce, Gd, La             | Cubic        | Fm-3m       | 74       | 7.220                                   | 7.035                         | a=5.468 (1)                                 |
| Perovskite in composite | La, Co, Ni Fe          | Orthorhombic | Pnma        | 26       | 7.010                                   | 6.864                         | a=5.5138 (3)<br>b=5.865 (5)<br>c=7.7851 (5) |

### 3.2. Electrochemical characterization.

Tietz et al. have reported very high electronic conductivity of LCNF up to 850 °C (ca. 512 S·cm<sup>-1</sup> at 800 °C). [29] Thus, the combination in a composite should provide the electronic conductivity that CGO20 lacks. Figure 3 presents the Arrhenius plot of LCNF, CGO20, LCNF-(La)CGO20 and LCNF-(La)CGO20-Ni(Co)O measured during cooling of the samples in air. In the present work, the conductivity observed for LCNF was 244.6 S·cm<sup>-1</sup> at 800 °C and this lower value is attributed to the remaining porosity. This would be in agreement with the findings observed by Rachadel et al., with an electrical conductivity reduction of 33% in a BSCF sample presenting a porosity of 35%. [32] The composite material shows high electrical conductivity (7.25 at 800 °C for LCNF-(La)CGO20-Ni(Co)O, and 2.6 S cm<sup>-1</sup> at 800 °C for LCNF-(La)CGO20), but notably lower than the LCNF. The decrease in conductivity may stem from i) the mixture with the fluorite and therefore distinct nature of the LCNF-LCNF or CGO-LCNF grain boundaries within the composite, blocking the ionic or electronic transport, and ii) differences in the perovskite lattice composition due to the cation migration either during the one-pot synthesis that causes the

decomposition of the perovskite in a perovskite and a rock salt phases, or during the later sintering process. Nevertheless, the electronic conductivity is two orders of magnitude higher than the ionic conductivity that will remain the limiting factor for the oxygen permeation. The activation energies of the composites with and without the Ni(Co)O third phase are 23.2 kJ mol<sup>-1</sup> (0.24 eV) and 25.1 kJ mol<sup>-1</sup> (0.26 eV), respectively. Those are higher than LCNF, which was 13.25 kJ mol<sup>-1</sup> (0.14 eV, also higher in this work than in the literature [29]) and lower than for CGO20 76.9 kJ mol<sup>-1</sup> (0.8 eV). The changes in activation energy indicate changes in the charge formation and mobility of major carrier (electron or electronic hole) for the different compositions of the composites.

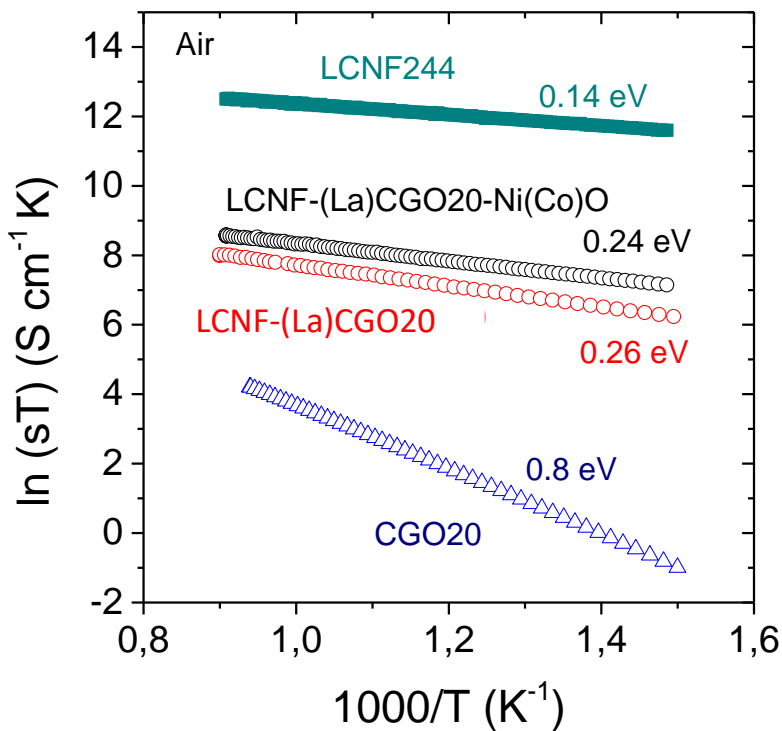


**Figure 3.** Arrhenius plot of the total conductivity of LCNF, CGO20, LCNF-(La)CGO20 and LCNF-(La)CGO20-Ni(Co)O in air.

### 3.3. Oxygen permeation measurements.

Temperature dependence on oxygen permeation was studied in the range 1000-700 °C under Air/Argon gradient, when feeding with 300 ml·min<sup>-1</sup> of synthetic air and 300 ml·min<sup>-1</sup> of Argon. Three different 0.6 mm-thick membranes were characterized: (i) a bare LCNF-(La)CGO20-

Ni(Co)O, and (ii) a bare and (iii) a CGO-LSM-activated LCNF-(La)CGO20 membrane. A maximum oxygen flux,  $J(O_2)$ , of  $0.74 \text{ ml}\cdot\text{min}^{-1}\cdot\text{cm}^{-2}$  is obtained at  $1000 \text{ }^\circ\text{C}$  for the activated LCNF-(La)CGO20 membrane. As can be seen in Figure 4, this composite membrane follows a 2-fold Arrhenius behavior, with a change in activation energy at  $800 \text{ }^\circ\text{C}$ . The actual results are also compared with previously studied membranes made of 50/50 vol%  $\text{Fe}_2\text{NiO}_4\text{-Ce}_{0.8}\text{Tb}_{0.2}\text{O}_{2-x}$  (NFO-CTO) also activated with the same CGO-LSM porous layer, as a reference of stable material. [10, 25] The non-activated LCNF-(La)CGO20-Ni(Co)O membrane displays better performance than the CGO-LSM-activated NFO-CTO membrane all along the studied temperature range ( $0.33 \text{ ml}\cdot\text{min}^{-1}\cdot\text{cm}^{-2}$  at  $1000 \text{ }^\circ\text{C}$ ). [25] This can be ascribed to the higher ionic conductivity of the CGO20 regarding the CTO. At temperatures below  $800 \text{ }^\circ\text{C}$ ,  $J(O_2)$  presents an apparent activation energy similar to those shown by activated membranes, attributed to the high electrical conductivity that ameliorates surface exchange steps in the triple phase boundaries at low temperatures. Finally, the great promotion effect of the activation layer in the LCNF-(La)CGO20 membrane should be highlighted, e.g. a 4-fold increase in  $J(O_2)$  is observed at  $850 \text{ }^\circ\text{C}$ .

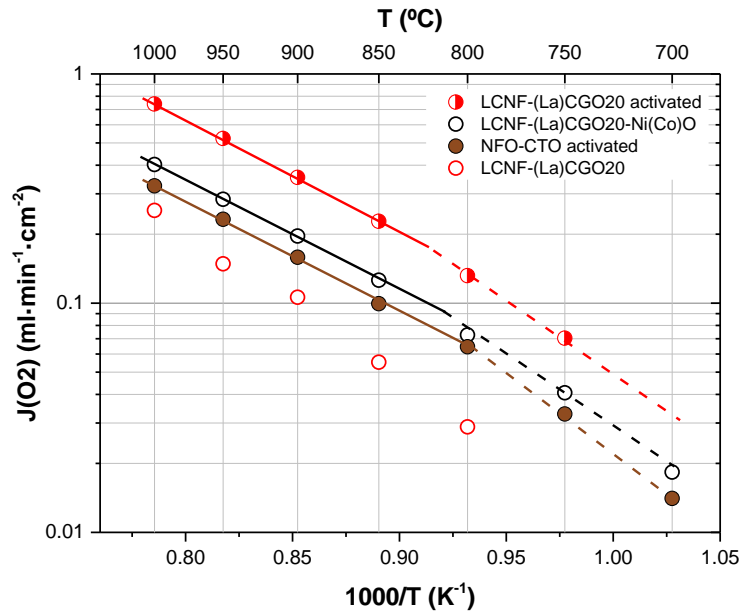


**Figure 4:** Temperature dependence of LCNF-CGO20 oxygen permeation in Ar sweep. Comparison with stable reference material NFO-CTO [25].

LCNF-(La)CGO20 activated and LCNF-(La)CGO20-Ni(Co)O membranes were also tested under different gas environments in the temperature range 1000-800 °C by means of sweep gas composition variation. Three different atmospheres were considered: (i) Ar (mimicking vacuum system extraction), (ii) 30% CO<sub>2</sub> in Ar and (iii) 250 ppm of SO<sub>2</sub> in 30% CO<sub>2</sub> in Ar, the two latter reproducing oxyfuel-like conditions. Each atmosphere was maintained during 120 minutes at every given temperature (1000, 950, 900, 850, 800 °C and 750 °C) following these steps: Ar, 30% CO<sub>2</sub> in Ar, 250 ppm in SO<sub>2</sub> in 30% CO<sub>2</sub> in Ar, and finally back to Ar sweeping. The reason for this procedure is to study the effect on oxygen permeation under CO<sub>2</sub> and SO<sub>2</sub>-containing atmospheres, and if the initial  $J(O_2)$  is recovered after SO<sub>2</sub> exposure. The results from these tests are shown in Figure 5a for LCNF-(La)CGO20 activated membrane, and in Figure 5b for LCNF-(La)CGO20-Ni(Co)O membrane, where oxygen fluxes are displayed in dependence of time for the different considered atmospheres and temperatures. Figure 5c is built from Fig. 5a and b taking the  $J(O_2)$  after stabilization values at every given temperature and gas condition, thus representing oxygen fluxes as a function of temperature. Fig. 5a and b shows that CO<sub>2</sub> presence improves oxygen permeation above 850 °C., with an increase from 0.66 to 0.71 ml·min<sup>-1</sup>·cm<sup>-2</sup> at 1000 °C when switching from pure Ar to 30% CO<sub>2</sub> in Ar sweeping for the activated membrane (Fig. 5a). Otherwise, below this temperature oxygen fluxes decrease when CO<sub>2</sub> is added to the sweep, being this worsening more evident the lower the temperature. This can be related to the better sweeping properties of CO<sub>2</sub> in comparison to Ar at these temperatures, i.e. an enhancement of flow-dynamics (use of CO<sub>2</sub> increases Reynolds number –see Fig. S3–, thus improving stream sweeping capacity that subsequently facilitates O<sub>2</sub> desorption from membrane surface). Moreover, the higher emissivity of CO<sub>2</sub> molecule can induce a locally-higher temperature on membrane surface, thus improving  $J(O_2)$ . CO<sub>2</sub>-O<sub>2</sub> competitive adsorption is neglected at these temperatures and apparently is not affecting negatively the overall oxygen permeation process. On the contrary, at temperatures below 850 °C, competitive adsorption becomes important and finally rate-limiting with decreasing temperatures, as inferred from the inferior  $J(O_2)$  values

achieved in CO<sub>2</sub>. Regarding SO<sub>2</sub> effect on permeation, under SO<sub>2</sub>-bearing atmosphere  $J(O_2)$  significantly drops, being more dramatic as temperature decreases. The latter can be ascribed to: (i) SO<sub>2</sub> adsorption in oxygen permeation active sites, in a similar way than the produced in the CO<sub>2</sub>-O<sub>2</sub> competitive adsorption, but with much stronger magnitude, and/or (ii) chemical reaction with membrane materials leading to structural changes, and secondary phases formation that can affect negatively oxygen permeation. As can be seen in Figure 5a and b for both studied membranes, SO<sub>2</sub> exposure produces a sudden and significant  $J(O_2)$  loss. Despite this dramatic drop, oxygen fluxes seem to be stabilized after a few minutes on stream. After SO<sub>2</sub> exposure, initial oxygen fluxes are recovered when switching back to Ar sweeping for both membranes at temperatures above 900 °C. Nevertheless, at 900 °C and lower temperatures the original  $J(O_2)$  before SO<sub>2</sub> exposure is not fully recovered. This can be due to a strong SO<sub>2</sub> adsorption at lower temperatures or due to the irreversible reaction affecting material structure.

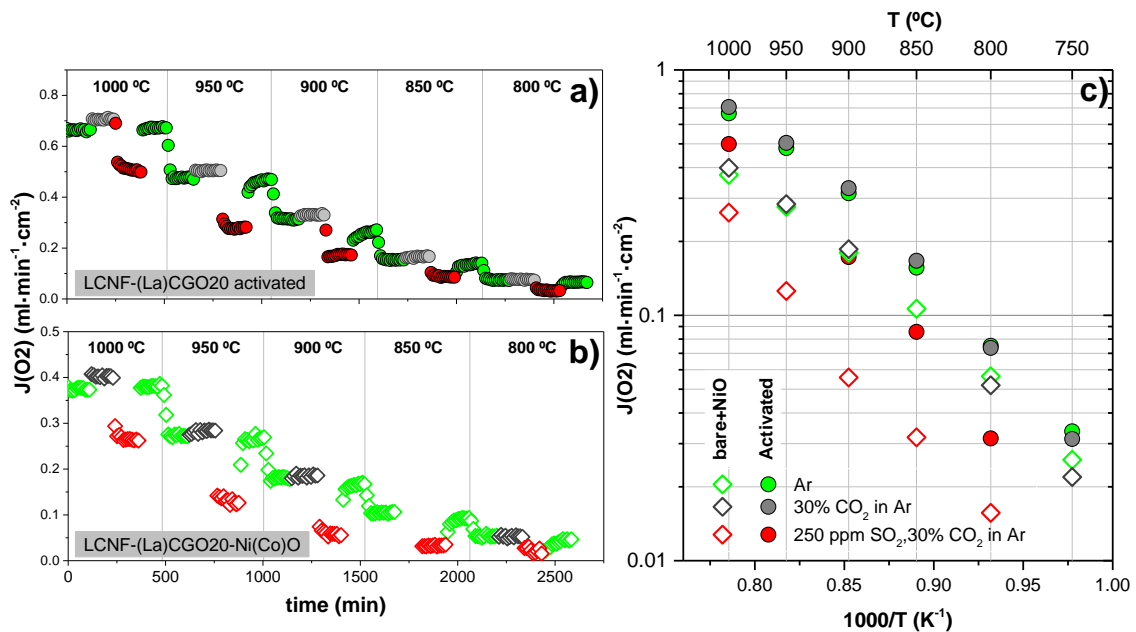


**Figure 5.** Time evolution of the membranes permeation flux upon variation of temperature and composition of the sweep gas stream for a) the LCNF-(La)CGO20 activated membrane and b) the LCNF-(La)CGO20-Ni(Co)O membrane, c) Arrhenius plot of the oxygen permeation under different environments for the two considered composite membranes, graph built from Figures a and b.

Activated LCNF-(La)CGO20 and LCNF-(La)CGO20-Ni(Co)O membranes were characterized after permeation testing in order to study possible material changes when exposed to Air/CO<sub>2</sub>-SO<sub>2</sub> gradients. Figure 6 shows FESEM analyses corresponding to LCNF-(La)CGO20 activated membrane. In Fig. 6a is shown a cross-section view of the activated membrane on sweep side after CO<sub>2</sub> and SO<sub>2</sub> exposure during permeation tests. As it can be seen, no reaction on membrane-porous layer is observed, maintaining the structural integrity of both elements. Nevertheless, presence of S probably related to SrSO<sub>4</sub> formation was detected on CGO-LSM layer by EDX analysis. A surface view of a fresh membrane is depicted on Figure 6b, where perovskite (dark gray) and fluorite (light gray) phases are identifiable. In Figures 6c and d are shown BSD-SEM images of sweep and feed side surfaces, respectively. These have been taken from membrane surface areas where no CGO-LSM layer is deposited (in Supporting Information a description of an activated membrane is provided). By comparing fresh sample (Fig. 6b) with tested sample (Fig. 6c and d) it is possible to identify the material changes after testing. With regard to the surface exposed to CO<sub>2</sub> and SO<sub>2</sub> (Fig. 6c) it is observed a predominance of clear grains (fluorite phase) over dark gray grains (perovskite phase) in contrast with the initial morphology (Fig. 6b) where phase distribution is balanced. A more significant degradation is observed in feed side surface (Fig. 6d), with the generation of prism-shaped NiO grains and a collapsing of composite material into a porous structure. NiO particles were also observed in a membrane cross section region near feed side (darker grains in Fig. 6e). The reason for the generation of NiO particles can be ascribed to the higher  $pO_2$  present in feed side environment, leading to the reaction of LCNF with the O<sub>2</sub> contained in the feed stream. The LCNF transformation after testing suggests that this material was not totally stabilized after calcination and forms more NiO when exposed to high- $pO_2$  environments. As a consequence of this, and as previously seen in the first approach preparation, a decrease in the perovskite phase percentage and an increase in material porosity is produced. XRD patterns (Figure 7) taken on membrane activated surfaces do not show any phase transformation on both feed and sweep sides. This can be due to protection features provided by CGO-LSM layer, thus avoiding membrane phases to react with CO<sub>2</sub>-SO<sub>2</sub> atmospheres, as Fig. 6a suggests. Furthermore, membrane XRD analysis through the 30  $\mu\text{m}$ -thick CGO-LSM can difficult

the identification of the small NiO grains observed by FESEM, since no additional peaks to LCNF, CGO and LSM are observed in feed side XRD results (Fig. 7).

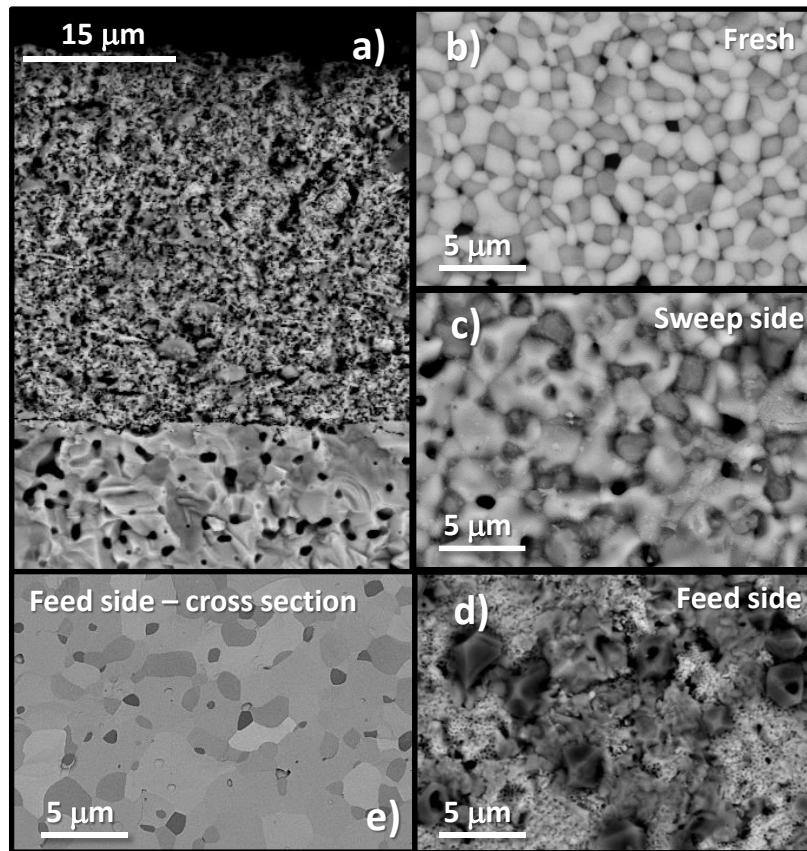


**Figure 6.** a) SEM cross-section view of a membrane activated with a CGO-LSM porous layer. BSD-SEM surface views of b) LCNFO-(La)CGO20 fresh membrane, c) sweep side after testing, d) feed side after testing, and e) BSD-SEM cross-section view of a tested membrane near feed side.

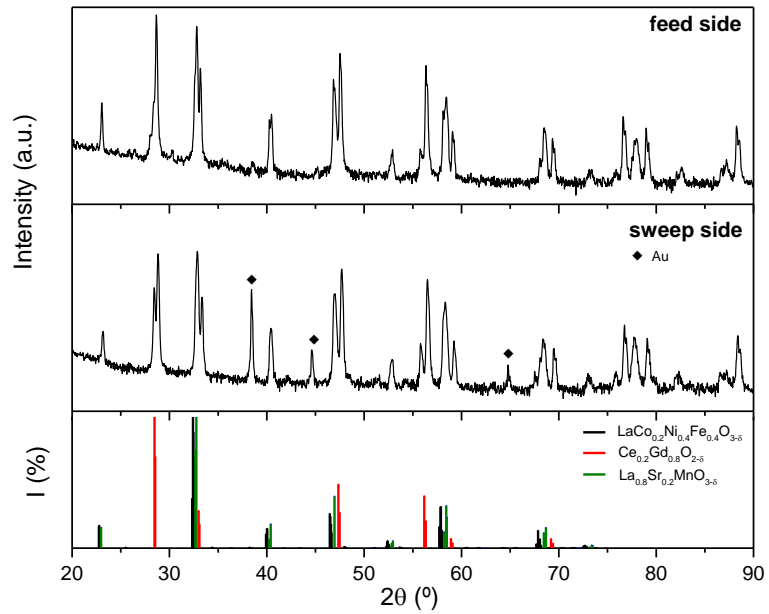


**Figure 7.** XRD patterns of the activated LCNF-(La)CGO20 membrane at feed and sweep sides after testing. Signal peak belonging to Au corresponds to the material used for sealing the membrane.

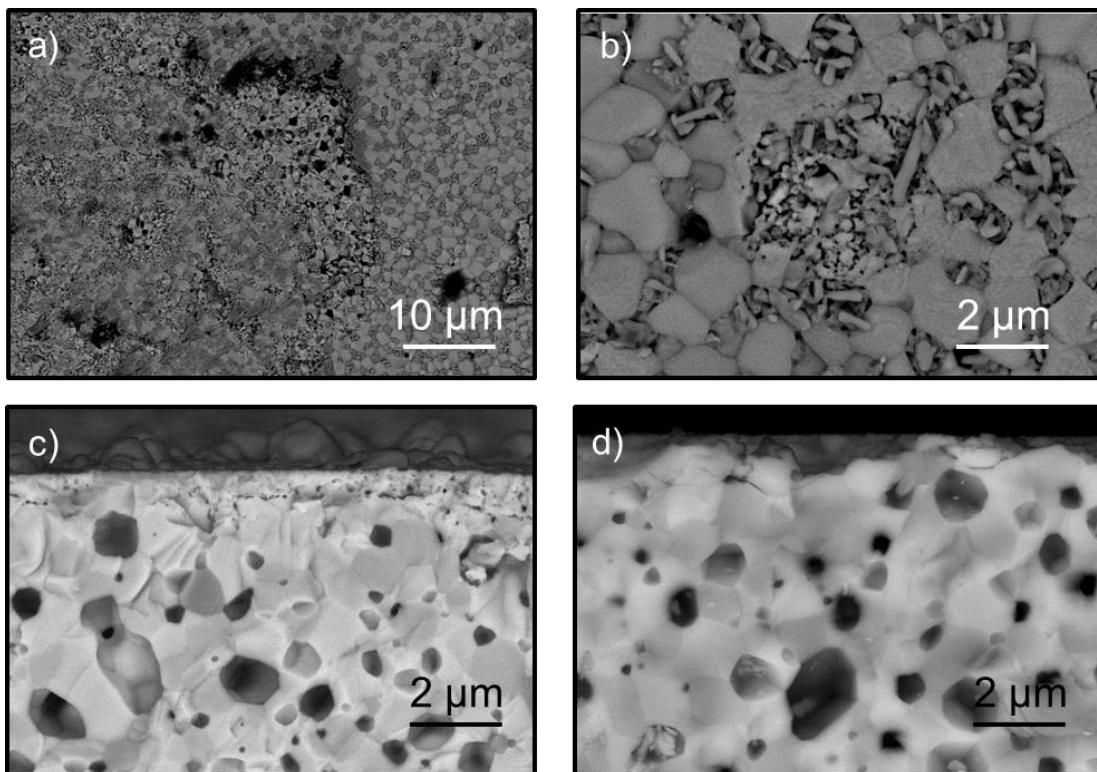


**Figure 8.** FE-SEM BS-images of LCNF-(La)CGO20-Ni(Co)O membrane, (a) and (b) sweep side surface, (c) fracture cross-section close to sweep-side surface, and (d) fracture cross-section close to feed-side surface.

FE-SEM analysis of the spent LCNF-(La)CGO20-Ni(Co)O membrane reveals that the membrane surface is degraded after the CO<sub>2</sub>-SO<sub>2</sub> exposition. Figure 8a and b evidence that SO<sub>2</sub> preferentially reacts with rock salt and perovskite phases. The rod-like particles on the surface correspond to the ceria phase and show traces of S, as detected by EDS (see Figure S5). These traces are probably sulfur compounds related to perovskite and rock salt phases decomposition, remaining on ceria grains after the material around is decomposed. The cross-sections in Figures 8c and d correspond to sweep (CO<sub>2</sub>-SO<sub>2</sub>) and feed (air) sides. The sweep side surface of the membrane is clearly degraded, forming a porous layer of ca. 500 nm with remaining features of the stable phase on top, whereas the feed side in contact with air remains unchanged. The fact that LCNF-(La)CGO20-Ni(Co)O sweep side (Fig. 8a and b) is more affected by degradation than LCNF-(La)CGO20 sweep side (Fig. 6c) can be ascribed to the presence of Ni(Co)O phase on the first, which reacts under SO<sub>2</sub>-containing atmospheres. Otherwise, LCNF-(La)CGO20-Ni(Co)O feed side appears unaltered in contrast to LCNF-(La)CGO20 membrane, which reacts forming NiO particles and producing a degradation of the surface. This is not occurring for the LCNF-(La)CGO20-Ni(Co)O membrane due to its initial Ni(Co)O content, thus avoiding any phase reaction and the subsequent structural degradation.

After changing from SO<sub>2</sub> to Ar, the surface is cleaned from sulfur. The oxygen flux is recovered as the inside of the membrane is still unchanged, but thinner and with a porous layer on top of the sweep side that compensates losses due to initial degradation.

#### **4. Conclusions.**

Dual-phase membranes based on mixtures of the perovskite LaCo<sub>0.2</sub>Ni<sub>0.4</sub>Fe<sub>0.4</sub>O<sub>3-δ</sub> (LCNF) and the fluorite Ce<sub>0.8</sub>Gd<sub>0.2</sub>O<sub>2-δ</sub> (CGO20) are developed and tested for oxygen separation at high temperature. Different approaches on the composite formation have been tested. The direct one-pot synthesis using Pechini route is not possible due to the formation of a NiO-based (rock-salt) secondary phase. The physical mixture of the separated highly-crystalline phase and later controlled firing at temperatures below 1460 °C enables to form the clean dual-phase composite.

Nevertheless, some interdiffusion occurs during sintering since La is detected in the fluorite phase, and longer oxidation periods, even at lower temperature produce the rock salt phase formation.

LCNF presents outstanding electronic conductivity at high temperature. The conductivity of the composite with no impurities is slightly higher (value at 800 °C) than the one observed for the composite with initial rock salt phase, 7.25 S cm<sup>-1</sup> versus 2.6 S cm<sup>-1</sup> at 800 °C .

Oxygen permeation studies show that, when no surface activation is realized, the membrane with higher total conductivity presents higher flux. On the other hand, when a porous mixed ionic-electronic porous activation is deposited on the membrane surface, the oxygen permeation is boosted, achieving a 4-fold improvement in flux at 850 °C. This composite presents one of the highest fluxes reported under clean conditions for monolithic dual-phase membranes. As a final step, the stability of the membrane was assessed under operation conditions. SO<sub>2</sub> reacts with LCNF elements and progressively forms secondary phases on the membrane surface. The activation layer also works as a protective layer to preserve the surface stability. On the other membrane side, it appears that the LCNF perovskite tends to demix and partly decomposes under very low pO<sub>2</sub> conditions found in the sweep side.

## **Acknowledgments**

Financial support by the Spanish Government (ENE2014-57651 and SEV-2016-0683 grants), by the EU through FP7 GREEN-CC Project (GA 608524), and by the Helmholtz Association of German Research Centers through the Helmholtz Portfolio MEM-BRAIN is gratefully acknowledged.

## **REFERENCES**

- [1] N. MacDowell, N. Florin, A. Buchard, J. Hallett, A. Galindo, G. Jackson, C.S. Adjiman, C.K. Williams, N. Shah, P. Fennell, An overview of CO<sub>2</sub> capture technologies, *Energy & Environmental Science*, 3 (2010) 1645-1669.
- [2] J. Garcia-Fayos, V.B. Vert, M. Balaguer, C. Solís, C. Gaudillere, J.M. Serra, Oxygen transport membranes in a biomass/coal combined strategy for reducing CO<sub>2</sub> emissions: Permeation study of selected membranes under different CO<sub>2</sub>-rich atmospheres, *Catalysis Today*, 257, Part 2 (2015) 221-228.
- [3] S.P.S. Badwal, F.T. Ciacchi, Ceramic Membrane Technologies for Oxygen Separation, *Advanced Materials*, 13 (2001) 993-996.
- [4] X. Dong, W. Jin, N. Xu, K. Li, Dense ceramic catalytic membranes and membrane reactors for energy and environmental applications, *Chemical Communications*, 47 (2011) 10886-10902.
- [5] Y. Wei, W. Yang, J. Caro, H. Wang, Dense ceramic oxygen permeable membranes and catalytic membrane reactors, *Chemical Engineering Journal*, 220 (2013) 185-203.
- [6] S.H. Morejudo, R. Zanon, S. Escolastico, I. Yuste-Tirados, H. Malerod-Fjeld, P.K. Vestre, W.G. Coors, A. Martinez, T. Norby, J.M. Serra, C. Kjolseth, Direct conversion of methane to aromatics in a catalytic co-ionic membrane reactor, *Science*, 353 (2016) 563-566.
- [7] J. Sunarso, S. Baumann, J.M. Serra, W.A. Meulenber, S. Liu, Y.S. Lin, J.C. Diniz da Costa, Mixed ionic, Ælectronic conducting (MIEC) ceramic-based membranes for oxygen separation, *Journal of Membrane Science*, 320 (2008) 13-41.
- [8] M.P. Lobera, J.M. Serra, S.P. Foghmoes, M. Sogaard, A. Kaiser, On the use of supported ceria membranes for oxyfuel process/syngas production, *Journal of Membrane Science*, 385 (2011) 154-161.
- [9] H. Stadler, F. Beggel, M. Habermehl, B. Persigehl, R. Kneer, M. Modigell, P. Jeschke, Oxyfuel coal combustion by efficient integration of oxygen transport membranes, *International Journal of Greenhouse Gas Control*, 5 (2011) 7-15.
- [10] M. Balaguer, J. Garcia-Fayos, C. Solis, J.M. Serra, Fast Oxygen Separation Through SO<sub>2</sub>- and CO<sub>2</sub>-Stable Dual-Phase Membrane Based on NiFe<sub>2</sub>O<sub>4</sub>-Ce<sub>0.8</sub>Tb<sub>0.2</sub>O<sub>2-δ</sub>, *Chemistry of Materials*, 25 (2013) 4986-4993.
- [11] H. Luo, K. Efimov, H. Jiang, A. Feldhoff, H. Wang, J. Caro, CO<sub>2</sub>-Stable and Cobalt-Free Dual-Phase Membrane for Oxygen Separation, *Angewandte Chemie International Edition*, 50 (2011) 759-763.
- [12] X. Zhu, H. Liu, Y. Cong, W. Yang, Novel dual-phase membranes for CO<sub>2</sub> capture via an oxyfuel route, *Chemical Communications*, 48 (2012) 251-253.
- [13] T.J. Mazanec, T.L. Cable, J.G. Frye Jr, Electrocatalytic cells for chemical reaction, *Solid State Ionics*, 53–56, Part 1 (1992) 111-118.
- [14] C.S. Chen, H. Kruidhof, H.J.W. Bouwmeester, H. Verweij, A.J. Burggraaf, Oxygen permeation through oxygen ion oxide-noble metal dual phase composites, *Solid State Ionics*, 86-88 (1996) 569-572.
- [15] C.S. Chen, A.J. Burggraaf, Stabilized bismuth oxide, Ænoble metal mixed conducting composites as high temperature oxygen separation membranes, *Journal of Applied Electrochemistry*, 29 (1999) 355-360.
- [16] U. Nigge, H.D. Wiemh√ ∂ fer, E.W.J. R√ ∂ mer, H.J.M. Bouwmeester, T.R. Schulte, Composites of Ce<sub>0.8</sub>Gd<sub>0.2</sub>O<sub>1.9</sub> and Gd<sub>0.7</sub>Ca<sub>0.3</sub>CoO<sub>3</sub>, ÆŒ as oxygen permeable membranes for exhaust gas sensors, *Solid State Ionics*, 146 (2002) 163-174.
- [17] A.L. Shaula, V.V. Kharton, F.M.B. Marques, A.V. Kovalevsky, A.P. Viskup, E.N. Naumovich, Oxygen permeability of mixed-conducting composite membranes: effects of phase interaction, *J. Solid State Electrochem.*, 10 (2006) 28-40.
- [18] M. Balaguer, C. Solís, J.M. Serra, Structural–Transport Properties Relationships on Ce<sub>1–x</sub>Ln<sub>x</sub>O<sub>2–δ</sub> System (Ln = Gd, La, Tb, Pr, Eu, Er, Yb, Nd) and Effect of Cobalt Addition, *The Journal of Physical Chemistry C*, 116 (2012) 7975-7982.

- [19] M. Balaguer, C. Solis, J.M. Serra, Study of the Transport Properties of the Mixed Ionic Electronic Conductor  $Ce_{1-x}Tb_xO_{2-d} + Co$  ( $x = 0.1, 0.2$ ) and Evaluation As Oxygen-Transport Membrane, *Chemistry of Materials*, 23 (2011) 2333-2343.
- [20] J. Yi, Y. Zuo, W. Liu, L. Winnubst, C. Chen, Oxygen permeation through a  $Ce_{0.8}Sm_{0.2}O_{2-\delta}$ - $La_{0.8}Sr_{0.2}CrO_{3-\delta}$  dual-phase composite membrane, *J. Membr. Sci.*, 280 (2006) 849-855.
- [21] H. Takamura, K. Okumura, Y. Koshino, A. Kamegawa, M. Okada, Oxygen permeation properties of ceria-ferrite-based composites, *J. Electroceram.*, 13 (2004) 613-618.
- [22] H. Takamura, T. Kobayashi, T. Kasahara, A. Kamegawa, M. Okada, Oxygen permeation and methane reforming properties of ceria-based composite membranes, *J. Alloys Compd.*, 408-412 (2006) 1084-1089.
- [23] S. Ovtar, J. Gorauskis, A.B. Haugen, C. Chatzichristodoulou, A. Kaiser, P.V. Hendriksen, Oxygen transport properties of tubular  $Ce_{0.9}Gd_{0.1}O_{1.95}$ - $La_{0.6}Sr_{0.4}FeO_{3-\delta}$  composite asymmetric oxygen permeation membranes supported on magnesium oxide, *Journal of Membrane Science*, 523 (2017) 576-587.
- [24] Z. Cao, X. Zhu, W. Li, B. Xu, L. Yang, W. Yang, Asymmetric dual-phase membranes prepared via tape-casting and co-lamination for oxygen permeation, *Materials Letters*, 147 (2015) 88-91.
- [25] J. Garcia - Fayos, M. Balaguer, J.M. Serra, Dual - Phase Oxygen Transport Membranes for Stable Operation in Environments Containing Carbon Dioxide and Sulfur Dioxide, *ChemSusChem*, 8 (2015) 4242-4249.
- [26] C. Gaudillere, J. Garcia-Fayos, M. Balaguer, J.M. Serra, Enhanced Oxygen Separation through Robust Freeze-Cast Bilayered Dual-Phase Membranes, *Chemsuschem*, 7 (2014) 2554-2561.
- [27] H. Falcón, A.E. Goeta, G. Punte, R.E. Carbonio, Crystal Structure Refinement and Stability of  $LaFe_xNi_{1-x}O_3$  Solid Solutions, *Journal of Solid State Chemistry*, 133 (1997) 379-385.
- [28] E.A. Kiselev, V.A. Cherepanov,  $p(O_2)$ -stability of  $LaFe_{1-x}Ni_xO_{3-\delta}$  solid solutions at 1100 °C, *Journal of Solid State Chemistry*, 183 (2010) 1992-1997.
- [29] F. Tietz, I. Arul Raj, Q. Ma, S. Baumann, A. Mahmoud, R.P. Hermann, Material properties of perovskites in the quasi-ternary system  $LaFeO_3$ - $LaCoO_3$ - $LaNiO_3$ , *Journal of Solid State Chemistry*, 237 (2016) 183-191.
- [30] M. Yashima, T. Takizawa, Atomic Displacement Parameters of Ceria Doped with Rare-Earth Oxide  $Ce_{0.8}R_{0.2}O_{1.9}$  ( $R = La, Nd, Sm, Gd, Y, \text{ and } Yb$ ) and Correlation with Oxide-Ion Conductivity, *The Journal of Physical Chemistry C*, 114 (2010) 2385-2392.
- [31] V.V. Kharton, A.V. Kovalevsky, A.P. Viskup, A.L. Shaula, F.M. Figueiredo, E.N. Naumovich, F.M.B. Marques, Oxygen transport in  $Ce_{0.8}Gd_{0.2}O_{2-\delta}$ -based composite membranes, *Solid State Ionics*, 160 (2003) 247-258.
- [32] P.L. Rachadel, J. Motuzas, G. Ji, D. Hotza, J.C. Diniz da Costa, The effect of non-ionic porous domains on supported  $Ba_{0.5}Sr_{0.5}Co_{0.8}Fe_{0.2}O_{3-\delta}$  membranes for  $O_2$  separation, *Journal of Membrane Science*, 454 (2014) 382-389.